Modeling two-dimensional crystals and nanotubes with defects under stress

Jürgen Dietel
Institut für Theoretische Physik, Freie Universität Berlin, Arnimallee 14, D-14195 Berlin, Germany

Hagen Kleinert
Institut für Theoretische Physik, Freie Universität Berlin, Arnimallee 14, D-14195 Berlin, Germany
and ICRANeT, Piazzale della Repubblica 1, 10-65122 Pescara, Italy

(Received 7 December 2008; revised manuscript received 5 May 2009; published 12 June 2009)

We calculate analytically the phase diagram of a two-dimensional planar crystal and its wrapped version with defects under external homogeneous stress as a function of temperature using a simple elastic square lattice model that allows for defect formation. The temperature dependence turns out to be very weak. The results are relevant for recent stress experiments on carbon nanotubes at high temperatures. Under increasing stress, we find a crossover regime which we identify with a cracking transition that is almost independent of temperature. Furthermore, we find an almost stress-independent melting point. In addition, we derive an enhanced ductility with relative strains before cracking between 200% and 400%, in agreement with carbon nanotube experiments. The specific values depend on the Poisson ratio and the angle between the external force and the crystal axes. We give arguments that the results for carbon nanotubes should be not much different from these results in spite of the different lattice structures.

DOI: 10.1103/PhysRevB.79.245415 PACS number(s): 62.20.F−, 61.46.Fg, 61.72.Lk, 64.70.dm

I. INTRODUCTION

The discovery of macroscopic two-dimensional (2D) graphene sheets obtained by mechanical cleavaging[1] has demonstrated that free-standing or suspended 2D crystals can exist despite their large in-plane positional fluctuations. Since then, a variety of other free-standing 2D crystallites have been prepared.[2] These crystals are stabilized by out-of-plane fluctuations as verified experimentally in Ref. 3, following the predictions in Ref. 4. The wrapped version of the 2D free-standing graphene had been found much earlier in 1991.[5] Due to their high strength, the mechanical properties of such materials have recently attracted great interest.

The behavior of three-dimensional (3D) crystals as a function of stress is well known. For small stresses, they expand elastically with a linear stress-strain curve. Above the yield point, the curve flattens due to the irreversible plastic deformation. At even higher stress, cleavage sets in with further fracture. If the plastic region is small or absent, the material is called *brittle*, otherwise *ductile*.

A similar stress-strain curve was expected for 2D crystals or their wrapped versions. Yakobson *et al.*[6] was one of the first to determine the cracking strain of single-wall carbon nanotubes (SWNTs) by computer simulation. Since then many similar studies have been carried out using different simulation methods (see Ref. 7 and references therein). Most of these observed a cracking strain between 15% and 40% depending on the chirality of the tube at room temperature $T \approx 300$ K. The results of the different simulations differ widely. Experimental values for ropes of SWNTs found cracking strains of 6% (Refs. 8 and 9) and 13% (Ref. 10) for multiwall nanotubes. Huang *et al.*[11] measured less than 15% for tensile failure at 300 K which is defined either by the yielding strain for ductile nanotubes or by the cracking strain for brittle ones. At high temperatures they were able to go to extreme elongations of 270% before cracking. Due to the large temperature, the SWNTs show an extremely ductile behavior with kink motion along the tubes. These were interpreted as defects which do not only perform glide but also climb motion in the SWNT (Refs. 12 and 13) at high temperatures. In Ref. 14, a molecular-dynamics simulation for various SWNTs at high temperatures was performed exhibiting large defect formations before cracking.

As a consequence of large activation barriers, the strain value of the yield point is mostly dominated by the creation of closely lying defect pairs of opposite "charge" forming dipoles at low temperatures. The poles separate by glide motions at increasing temperatures. By calculating the energies of Stone-Wales (SW) defects one finds, by simulation, a strain value between 6% (armchair tube) and 12% (zigzag),[15–17] with these defects possessing negative formation energy. The results were consistent with experiments based on measuring electronic scattering in the tube.[18] Plastic behavior for various SWNTs is seen to set in at relative strains between 5% and 10%.

From numerical simulations, we know that the activation barriers for SW defects are quite large.[19–21] It depends on the time duration of stress or heat, how the SW defects form. For example, brittle SWNTs show a defect formation that leads immediately to cleavaging and subsequent cracking.

The purpose of this note is to study these processes with the help of an extension of a model introduced in Refs. 22 and 23 to describe crystal melting of 2D and 3D lattices. The model contains linear elastic forces coupled minimally to an additional integer-valued plastic field to allow for defect formation. This model is here extended by an external stress. By modifying this we can investigate phase transitions and instabilities of a 2D crystal under stress at finite temperatures. We shall restrict ourselves mainly to a square-lattice model and its wrapped version, for simplicity. The more realistic triangular and honeycomb lattices will be treated in the future by extending the corresponding melting models.[23] The basic physics will not be much different for different lattice symmetries. We come back to this point in Sec. VI below

where we give more arguments that also quantitatively it should not change much going from square crystals to triangular and honeycomb lattices and its wrapped versions.

The main advantage of square lattices is that one can easily calculate partition functions, which require sums over integer-valued defect fields. The sums are simplest for square crystals with small Poisson ratios.[22] It turns out that SWNTs and graphene are systems with small Poisson ratio of ~0.14, making them well suited for applying this technique. The sums can be performed with a technique developed for *XY* models of superfluidity, using the so-called inverse Villain (iV) approximation.[22] The defect model in this approximation will briefly be referred to as *cosine model*. In the cosine model, the defect aspects can be treated by mean-field methods.

In the following, we will first discuss the phase diagram of extended 2D square crystals starting with the phase diagram of the cosine model in mean-field approximation. We shall find a second-order phase transition line which is identified as the cracking transition connecting the melting point with a point at zero temperature. In addition, we encounter a vertical second-order transition line at constant temperature starting at the melting point.

Next, we discuss the full theory without the iV approximation. We shall find a similar phase diagram where now the second-order cracking line in the iV approximation is almost everywhere a crossover. For temperatures near the melting transition, our theory gives relative strains of 200–400 % before cracking. This is in accordance with the high-strain values of the experiments of Huang *et al.*[11,12] for SWNTs. We find extended defect configurations before cracking consisting of homogeneously distributed defect stripes.

Finally, we will discuss the physics of large wrapped square crystals under stress. We find the same phase diagram, stress-strain function, and cracking stress for the wrapped version of a square crystal as for the 2D extended crystal. The main difference lies in the fact that for *chiral* tubes, which we define by the property that the vector along the circumference of the square tube lies not in the direction of a crystal axis, show spiral-like defect configurations under stress. In accordance with the experiments[12] defect glide and climbs are relevant in tubes.

We point out that within our theory it is impossible to find the correct yield point at small temperatures where plasticity sets in, since our model does not really account for the true activation barriers.[19–21] Since activation energies at high temperatures are no longer relevant because defects overcome the barriers by thermal fluctuations, we expect that the yielding point tends to zero stress leading to an extensive dislocation creep seen in the experiments of Huang *et al.*[11] This is the temperature regime where our theory gives the correct phase diagram.

The paper is organized as follows. In Sec. II we state the model. Section III contains the calculation of the phase diagram within the iV approximation in mean field. In Sec. IV, we discuss the full crystal Villain model. Section V contains a discussion of the true phase diagram for a square crystal under stress by taking into account the discussions in Secs. III and IV. We also discuss in this section the cracking stress and the relative strains as functions of the external stress before cracking. In Sec. VI, we discuss the modifications of our results when considering wrapped versions of 2D crystals and carbon nanotubes

II. MODEL

The partition function used here for the square crystal was proposed in Ref. 22. It can be written in the canonical form as a functional integral,

$$Z_{\rm fl} = \int \mathcal{D}[u_i,\sigma_{ij},n_{ij}]e^{-(H_d[u_i,\sigma_{ij},n_i]+H^1_{\sigma^0}[u_i])/k_BT}, \tag{1}$$

where

$$\frac{H_d[u_i,\sigma_{ij},n_{ij}]}{k_BT} = \sum_{\mathbf{x}} \left\{ \frac{1}{2\beta}\left[\frac{1}{2}\sigma_{ij}^2 - \frac{\lambda}{4(\lambda+\mu)}\left(\frac{\bar{\nabla}_i}{\nabla_i}\sigma_{ii}\right)^2\right] - 2\pi i\sigma_{ij}(\nabla_i u_j + n_{ij}) \right\} \tag{2}$$

and

$$H^1_{\sigma^0}[u_i] = -v_F\sum_{\mathbf{x}} \sigma^0_{ij}\nabla_i u_j. \tag{3}$$

Here $v_F=a^2$ is the area of the fundamental cell where a is the lattice constant. The exponent in Eq. (1) contains the canonical representation of elastic and plastic energies, summed over the lattice sites $\mathbf{x}$ of a 2D lattice. The canonically conjugate variables of the distortion fields $\nabla_j u_i$ are the stress fields σ_{ij} for $i\leq j$ with the abbreviation $\sigma_{21}\equiv\sigma_{12}$.[22] The stress field σ^0_{ij} accounts for external forces applied to the boundary of the crystal. The parameter β is proportional to the inverse temperature, $\beta\equiv a^2\mu/k_BT(2\pi)^2$.

The integer-valued fields $n_{ij}(\mathbf{x})$ in Eq. (2) are defect gauge fields representing the jumps of the displacements field $u_i(\mathbf{x})$ over the *Volterra surfaces*. The lattice derivatives ∇_i and their conjugate counterparts $\bar{\nabla}_i$ denote lattice differences for a cubic 2D crystal. In Eq. (2), the defect gauge fields n_{ij} is coupled minimally to the displacements fields u_i. Note that we do not have this minimally coupling in the stress term $H^1_{\sigma^0}[u_i]$ because the external force only acts on the surface of the crystal.

The measure of functional integration in Eq. (1) is

$$\int \mathcal{D}[u_i,\sigma_{ij},n_{ij}] = \left[\frac{\mu}{4(\lambda+\mu)}\right]^{N/2}\left[\frac{1}{2\pi\beta}\right]^{3N/2} \times\left\{\prod_{\mathbf{x}}\left[\prod_{i\leq j}\int_{-\infty}^{\infty}d\sigma_{ij}\right]\left[\prod_{ij}\sum_{n_{ij}(\mathbf{x})=-\infty}^{\infty}\right] \times\left[\int_{-\infty}^{\infty}\frac{d\mathbf{u}}{a}\right]\right\}, \tag{4}$$

where N is the number of lattice sites.

Let us integrate out the stress fields σ_{ij} in Eq. (1). This leads to the partition function of an elastic Hamiltonian with a minimally defect gauge field under stress.[22] We use *free boundary conditions* for the crystal. These are taken into

account by separating the displacements field integration in the partition function over zero-momentum terms $u_i(q=0)$ and terms with $u_i(q\neq 0)$.[24] In the following we first integrate out the zero-momentum displacement fields $u_i(q=0)$. One should now take care of this integration due to the following fact: a crystal which is homogeneously deformed has three independent strain directions instead of two which is suggested by the counting of the number of displacement fields. One can take care of this by integrating over the three independent strain fields $u_{ij}=(\nabla_i u_j+\nabla_j u_i)/2$ for $q=0$ (Ref. 24) instead of the displacement fields $u_i(q=0)$. This leads to the partition function

$$Z_{\mathrm{fl}}=\int \mathcal{D}[u_i,\sigma_{ij},n_{ij}]\exp\left[-\frac{(H_d[u_i,\sigma_{ij},n_i]+\tilde{H}^1_{\sigma^0}[u_i]+\tilde{H}^2_{\sigma^0})}{k_BT}\right], \tag{5}$$

with

$$\tilde{H}^1_{\sigma^0}[u_i]=v_F\sum_{\mathbf{x}}\sigma^0_{ij}(\nabla_i u_j+n_{ij}), \tag{6}$$

$$\tilde{H}^2_{\sigma^0}=-\frac{v_F}{\mu}\sum_{\mathbf{x}}\left[\frac{1}{4}(\sigma^0_{ij})^2-\frac{\lambda}{8(\lambda+\mu)}(\sigma^0_{ii})^2\right]. \tag{7}$$

The displacements fields $u_i(\mathbf{x})$ of nonzero momentum are integrated out in the integration measure (4) with *periodic boundary conditions*. Because of this, the first term in $\tilde{H}^1_{\sigma^0}[u_i]$ is actually zero for homogeneous external stress. It is only displayed in Eq. (6) to exhibit the minimal coupling nature of the defect fields in Eq. (5). The Hamiltonian $\tilde{H}^2_{\sigma^0}$ describes the well-known elastic energy of a 2D crystal under a constant stress if no defects are present. Due to its similarity with the Villain model of superfluidity,[22] model (5) will be called the *Villain model of crystals*.

III. SQUARE CRYSTAL IN COSINE MODEL

In the following, we restrict our attention to an external homogeneous stress along the x axis, i.e., $\sigma^0_{ij}=\sigma^0\delta_{i1}\delta_{j1}$. We shall calculate the partition function (1) in the iV approximation in mean field for $\nu=0$. This was done in the case of zero external stress in a textbook.[22]

We now describe the procedure when taking into account external stresses. First, we integrate out in Eq. (1) the stress fields σ_{ij}. Then one can sum in the iV approximation over the integer defect fields by restricting the displacements fields to the fundamental cell.[22] This leads up to structural factors being a function of a parameter $\beta_{\bar{V}}$ related to the parameter β by an inverse Villain transformation,[22]

$$\beta=-\frac{1}{2\ln[I_d(\beta_{\bar{V}})]}, \tag{8}$$

$$Z_{\mathrm{fl}}\sim\prod_{\mathbf{x}}\left[\int_{-a/2}^{a/2}\frac{d\mathbf{u}}{a}\right]\exp[-\beta_{\bar{V}}H^{XY}_d-2\tilde{H}^2_{\sigma^0}/k_BT], \tag{9}$$

with the cosine Hamiltonian

$$H^{XY}_d=-\sum_x\cos[2\pi(\nabla_1u_2+\nabla_2u_1)]+2\cos\left[2\pi\left(\nabla_1u_1+\frac{1}{2\mu}\sigma^0\right)\right]+2\cos[2\pi\nabla_2u_2]. \tag{10}$$

Here $I_d(\beta)$ is defined by $I_d(\beta)=I_1(\beta)/I_0(\beta)$ and I_0, I_1 are modified Bessel functions of the first kind. Over the relevant regime treated in this paper, $\beta_{\bar{V}}$ is roughly proportional to β.[22,25] The displacement fields satisfy periodic boundary conditions. Hamiltonian (10) represents two one-dimensional (1D) XY models which are coupled by the first term. This coupling term causes the melting transition for $\sigma^0=0$.[22]

There are two identical ways to derive a mean-field approximation from the partition function (10).[22] Either one uses the Bogoliubov variation principle with a trial Hamiltonian or one inserts constraint fields leading to the variational mean-field free energy f_{var} per atom in the lattice.[22] In the following we discuss the first way. As a trial partition function we use

$$Z_0=\prod_{\mathbf{x},i}\int_{-a/2}^{a/2}\frac{du_i(\mathbf{x})}{a}\exp\left[\alpha_i\cos\left(2\pi\frac{u_i(\mathbf{x})}{a}\right)\right]. \tag{11}$$

In general $\alpha_1\neq\alpha_2$ for an external stress which is not zero. In Ref. 22 one uses the same ansatz for the trial partition function where $\alpha_1=\alpha_2$ when the external stress is zero. By using Peierls inequality we obtain an upper bound for the actual free energy per lattice site $f_{\mathrm{fl}}=-k_BT\ln(Z_{\mathrm{fl}})/N$ (Ref. 22) given by f_{var} with

$$f_{\mathrm{var}}=-k_BT\Big\{\ln[I_0(\alpha_1)]+\ln[I_0(\alpha_2)]+\beta_{\bar{V}}I_d(\alpha_1)^2I_d(\alpha_2)^2+\beta_{\bar{V}}2\cos\left(\frac{\pi\sigma^0}{\mu}\right)I_d(\alpha_1)^2+\beta_{\bar{V}}2I_d(\alpha_2)^2-\alpha_1I_d(\alpha_1)-\alpha_2I_d(\alpha_2)\Big\}-\frac{v_F(\sigma^0)^2}{2\mu}. \tag{12}$$

The best approximation for f_{fl} is given by the minimum of f_{var} with respect to α_1,α_2. We mention that the first term in Eq. (10) corresponds to the third term in Eq. (12).

The analysis of the saddle point equations for Eq. (12) is straightforward. We summarize in the following the results briefly. We find four distinct solutions characterized by $\alpha_i=0$ or $\alpha_i\neq 0$ for $i=1,2$. Only three of these saddle point solutions are minima of f_{var} in certain (T,σ^0) regimes corresponding to phase regions. To be more specific, one can show that the saddle point with $\alpha_1\neq 0$, $\alpha_2=0$ is not a minimum of f_{var} when comparing its free-energy value with the other saddle point values. One obtains the following three different β_V regimes $\mathcal{R}_i$ as a function of σ^0:

$$\mathcal{R}_1:\beta_{\bar{V}}>\beta_{\bar{V},b}(\sigma^0),$$

$$\mathcal{R}_2:1/2\leq\beta_{\bar{V}}\leq\beta_{\bar{V},b}(\sigma^0),$$

$$\mathcal{R}_3: 1/2 > \beta_{\bar{V}}. \tag{13}$$

The function $\beta_{\bar{V},b}(\sigma^0)$ is defined by the implicit equations

$$\beta_{\bar{V},b} = \frac{\alpha}{4I_d(\alpha)},$$

$$\cos\left(\frac{\pi\sigma^0}{\mu}\right) = \frac{2}{\alpha}I_d(\alpha) - \frac{1}{2}I_d^2(\alpha). \tag{14}$$

The values of α_i in the regimes $\mathcal{R}_i$ are

$$\mathcal{R}_1: I_d(\alpha_1) = \sqrt{\frac{1}{2\beta_{\bar{V}}}\frac{\alpha_2}{I_d(\alpha_2)} - 2},$$

$$I_d(\alpha_2) = \sqrt{\frac{1}{2\beta_{\bar{V}}}\frac{\alpha_1}{I_d(\alpha_1)} - 2\cos\left(\frac{\pi\sigma^0}{\mu}\right)},$$

$$\mathcal{R}_2: \alpha_1 = 0, \quad 4\beta_{\bar{V}} = \frac{\alpha_2}{I_d(\alpha_2)},$$

$$\mathcal{R}_3: \alpha_1 = 0, \quad \alpha_2 = 0. \tag{15}$$

The free energies in the various regimes are given by

$$\mathcal{R}_1: f_{\rm var} = -k_BT\left\{\ln[I_0(\alpha_1)] + \ln[I_0(\alpha_2)] - \frac{\alpha_1}{2}I_d(\alpha_1) - \frac{\alpha_2}{2}I_d(\alpha_2) - \frac{\alpha_2}{2}\frac{I_d(\alpha_1)^2 I_d(\alpha_2)}{[2 + I_d(\alpha_1)^2]}\right\} - \frac{v_F(\sigma^0)^2}{2\mu},$$

$$\mathcal{R}_2: f_{\rm var} = -k_BT\left\{\ln[I_0(\alpha_2)] - \frac{\alpha_2}{2}I_d(\alpha_2)\right\} - \frac{v_F(\sigma^0)^2}{2\mu},$$

$$\mathcal{R}_3: f_{\rm var} = -\frac{v_F(\sigma^0)^2}{2\mu}. \tag{16}$$

In Fig. 1, we show the phase diagram calculated with the help of Eqs. (8), (13), (15), and (16). We obtain two second-order phase transitions between the three regions $\mathcal{R}_i$. The fact that the transition between $\mathcal{R}_1$ and $\mathcal{R}_2$ is of second-order type can be best seen by using the stationarity condition for $f_{\rm var}$ in the saddle point. This transition corresponds to the cracking transition. The transition line intersect the $1/\beta$ axis at the melting transition point $1/\beta_m$ corresponding to $1/\beta \approx 2.85$. On the low-temperature side, the transition line intersects the $\sigma^0/2\mu$ axis at $\sigma_b^0/2\mu = 1/3$. We note that in the regime $\mathcal{R}_2$ where $\alpha_1 = 0$ we obtain from Eq. (12) the mean-field variational energy of a 1D *XY* model. The second-order transition between $\mathcal{R}_2$ and $\mathcal{R}_3$ corresponds then to the phase transition of a 1D *XY* model obtained by the help of the mean-field approximation. In an exact treatment of the 1D *XY* model, this transition is of course not existent being only an artifact of the mean-field approximation.[26] There is in fact an argument that this phase transition for the 2D crystal under stresses is existent because for real physical systems there exists a melting transition beyond the cracking of the crystal. Note that we cannot get the cleavaged cracked state exactly within our model since in real physical systems the time scale beyond cracking is so long that the thermodynamical average is no longer fulfilled for a concrete system. Within our formalism, we can only describe the physics of the Gibb's state including a thermodynamical average. In the next section we shall discuss the full model (1) with Eq. (2) where we still find a melting transition independent of the external stress σ^0.

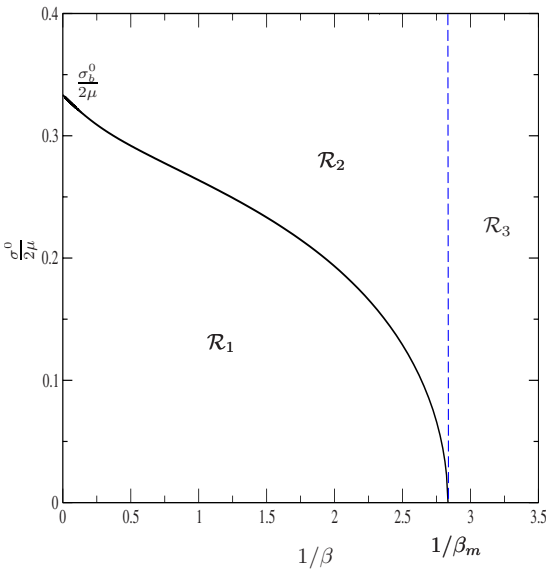

FIG. 1. (Color online) We show the phase diagram in the $(1/\beta, \sigma^0/2\mu)$ plane of a 2D crystal under stress σ^0 calculated in the mean-field iV approximation by using Eqs. (13), (15), and (16). The intersection of the transition lines and the temperature axis denoted by $1/\beta_m$ is the melting point for zero external stress.

Next, we calculate the relative strain parallel to the external force within the mean-field approximation of the cosine model. It is given by $\Delta u_\parallel/a = \partial f_{\rm var}/\partial(v_F\sigma^0)$. In Fig. 2 we show relative strain values for various dimensionless temperatures $1/\beta$ as a function of the external dimensionless stress $\sigma^0/2\mu$. The solid (black) curve shows two times the elastic part of the total relative strain, i.e., $2\sigma^0/2\mu$. We do not obtain from the mean-field approximation of the cosine model elongation rates before breaking of a few hundred percent seen in carbon nanotube experiments[11] but only less than 2/3. The reason lies presumably in the mean-field approximation which does not take into account the defect degrees of freedom correctly. This will be shown in the next section by taking into account the stress degrees of freedom in the full crystal Villain model exactly when calculating the free energy.

IV. SQUARE CRYSTAL IN VILLAIN MODEL

Next, we discuss the partition function (5) of the full models (6) and (7). The melting line of the 2D square crystal under the influence of homogeneous stress will be calculated similarly to the stress-free system.[22,23] This was done by intersecting the high- and low-temperature expansions of the partition function (5).

First, we calculate the simpler case of the high-temperature expansion. This was carried out formerly in

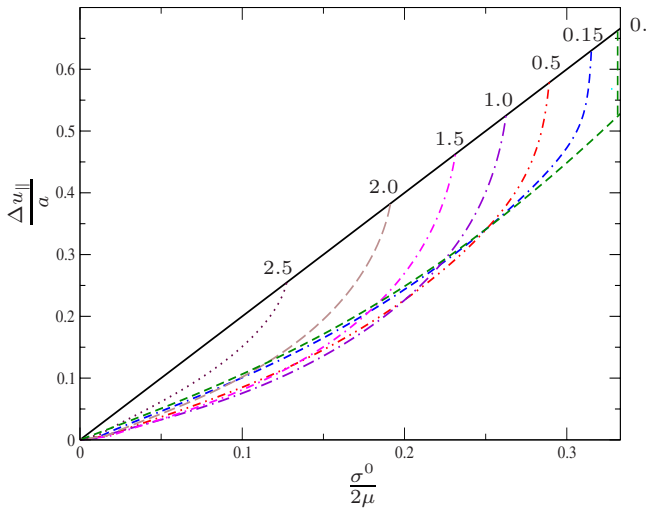

FIG. 2. (Color online) We show the relative elongation rates $\Delta u_\parallel/a$ in the direction of the external force as a function of the dimensionless external stress $\sigma^0/2\mu$. The (black) straight solid curve corresponds to two times the elastic elongation, i.e., $2\sigma^0/2\mu$. We show the elongation rates for various different dimensionless temperatures $1/\beta$ shown as numbers located at the intersection point of the corresponding curve with the (black) solid straight curve. The x-axis value of the intersection point is then given by the dimensionless cracking stress.

Ref. 22 for the case $\sigma^0_{ij}=0$. We start by integrating out in Eq. (5) the displacements fields u_i and afterward the stress field σ_{ij}. This leads us to the high-temperature limit of the partition function Z,

$$Z^{T\to\infty} = Z_0^{T\to\infty} e^{-2\tilde{H}^2_{\sigma^0}/k_BT} Z_{\text{stress}} \tag{17}$$

with

$$Z_{\text{stress}} = \prod_{\mathbf{x}} \left[\sum_{\chi(\mathbf{x})\in\mathbb{Z}} \right] \exp\left[-\frac{1}{4\tilde{\beta}} \sum_{\mathbf{x},\mathbf{x}'} \chi(\mathbf{x}) a^{-4} v^{-2}(\mathbf{x}-\mathbf{x}') \chi(\mathbf{x}') \right], \tag{18}$$

where $v(\mathbf{x})$ is short for $\Delta^{-1}(\mathbf{x})$ and $\Delta(\mathbf{x})$ is the 2D lattice Laplacian. $\tilde{\beta}$ is defined by $\tilde{\beta}\equiv\beta[1+\lambda/(2\mu+\lambda)]$ and we shall use further the abbreviation $\tilde{\mu}\equiv\mu[1+\lambda/(2\mu+\lambda)]$ below. The lowest-order approximation to the high-temperature partition function $Z_0^{T\to\infty}$ is given by[23]

$$Z_0^{T\to\infty} (2\pi\beta)^{-3N/2} \left[\frac{\mu}{4(\lambda+\mu)} \right]^{N/2}. \tag{19}$$

Taking only into account the dominant stress configuration $\chi(\mathbf{x})=\pm\delta_{\mathbf{x},\mathbf{x}_0}$, we obtain[23]

$$Z_{\text{stress}} \approx \exp[2Ne^{-5/\tilde{\beta}}]. \tag{20}$$

Note that we obtain an agreement between the free-energy densities in the high-temperature phase $\mathcal{R}_3$ (16) for the cosine model with the σ^0 part of the high-temperature free-energy density calculated from Eq. (17) which is given by $2\tilde{H}^2_{\sigma^0}/N$.

We now turn to the low-temperature expansion. For σ^0_{ij} =const one can skip the first term in Eq. (6) [we left this additional vanishing term only in Eq. (6) to show the minimal coupling form and thus the gauge degrees of freedom of the defect fields]. First, we integrate out the displacement fields u_i and afterward the stress fields σ_{ij}. This leads to a partition function of an elastic crystal under stress multiplied by a defect-dependent term denoted by Z_{def},

$$Z^{T\to 0} = Z_0^{T\to 0} e^{-\tilde{H}^2_{\sigma^0}/k_BT} Z_{\text{def}} \tag{21}$$

with the lowest-order result[22,23]

$$Z_0^{T\to 0} = (2\pi\beta)^{-N} \left(\frac{\mu}{\lambda+2\mu} \right)^{N/2} e^{-N\ell}, \tag{22}$$

where $\ell\approx 1.14$. The defect part of the low-temperature partition function is given by

$$Z_{\text{def}} = \sum_{\mathcal{S}} \sum_{n_{ij}\in\mathcal{S}} \exp\left[-\frac{1}{k_BT} (H_{\text{def}}[n] + H_{\sigma^0}[n]) \right], \tag{23}$$

with

$$\frac{H_{\text{def}}[n]}{k_BT} = 4\pi^2\tilde{\beta} \sum_{\mathbf{x},\mathbf{x}'} [\epsilon_{ii'}\nabla_i \epsilon_{jj'}\nabla_j n_{i'j'}(\mathbf{x})] v^2(\mathbf{x}-\mathbf{x}') \times [\epsilon_{kk'}\nabla'_k \epsilon_{ll'}\nabla'_l n_{k'l'}(\mathbf{x}')], \tag{24}$$

$$H_{\sigma^0}[n] = v_F \sum_{\mathbf{x}} \sigma^0_{ij}(\mathbf{x}) n_{ij}(\mathbf{x}). \tag{25}$$

The symbol $\mathcal{S}$ in Eq. (23) denotes the set of gauge-inequivalent defect configurations n_{ij} on the lattice which omit all gauge-equivalent versions $n'_{ij}=n_{ij}(\mathbf{x})+\nabla_i\lambda_j$ with periodic functions λ_i. The first term in Eq. (23) is a pure defect interaction energy term; the second term is a stress-defect interaction term. The latter results in the well-known Peach-Koehler force resulting from a defect configuration n_{ij} caused by the external stress.[27]

In the following, we choose $\sigma^0_{ij}=\sigma^0\delta_{i1}\delta_{j1}$ as in the last section and consider the following defect configuration:

$$n^l_{ij}(\mathbf{x}) = \pm\,\delta_{i,1}\delta_{j,1} \prod_{m=0}^{l} \delta_{\mathbf{x},am\mathbf{e}_2}. \tag{26}$$

From Eq. (24) we find that this defect configuration has an energy dependence $H_{\text{def}}[n^l]/k_BT\sim\ln(l)$. On the other hand the stress-defect energy term $H_{\sigma^0}[n^l]$ is proportional to the length of the defect line l, i.e., $H_{\sigma^0}[n^l]/k_BT\sim\pm l$. This means that for an infinite crystal one can construct localized defect configurations with arbitrarily small energies. This leads us to the conclusion that for high temperatures, where activation energies are no longer relevant, the yield point where plasticity sets in lies almost at zero stress.

The defects of the type n^l make the defect partition sum Z_{def} in Eq. (23) diverged, when performing the sum over all defect configurations in the free energy. Their contribution decreases with their geometric size in a *cluster expansion*. This is in contrast to the convergent sum for Z_{def} for $\sigma^0=0$ (23) due to the fact that large defect configurations have

generally large defect energies $H_{\rm def}$ (Refs. 22 and 23) and thus small Boltzmann factors. Mathematically speaking, one cannot interchange the cluster expansion sum of Eq. (23) with the thermodynamic limit $N\to\infty$ for $\sigma^0\neq 0$.

In order to calculate the free energy, we define the following defect fields:

$$\tilde{n}_{ij}(\mathbf{x}) = \sum_n (n_1 \delta_{x_1,ad_1n}\delta_{i,1}\delta_{j,1} + n_2 \delta_{x_2,ad_2n}\delta_{i,2}\delta_{j,2}). \quad (27)$$

The integer-valued numbers n_i, d_i are defined below. We now Fourier transform the defect fields $\tilde{n}_{ij}(\mathbf{x})$ leading for $N\to\infty$ to

$$\begin{aligned}\tilde{n}_{ij}(\mathbf{k}) &= \sum_{\mathbf{x}} \tilde{n}_{ij}(\mathbf{x}) e^{-i\mathbf{kx}} \\ &= (2\pi)^2 \sum_{n_1,n_2} \delta_{i,1}\delta_{j,1}\delta(ad_1k_1 - 2\pi n_1)\delta(ak_2 - 2\pi n_2) \\ &\quad + \delta_{i,2}\delta_{j,2}\delta(ak_1 - 2\pi n_1)\delta(ad_2k_2 - 2\pi n_2). \end{aligned} \quad (28)$$

In the following, we substitute $n_{ij}\to n_{ij}+\tilde{n}_{ij}$ in Eq. (23). The aim is to choose n_i, d_i in such a way that the terms proportional $\Sigma_{\mathbf{x}}\sigma^0_{ij}n_{ij}$ vanish in the exponent of Eq. (23). From Eq. (24) we obtain only nonvanishing contributions of the n_1, n_2 sum in Eq. (28) for $n_1=n_2=0$. In order to obtain the correct result we have to be rather careful in taking the zero-momentum limits in Eq. (24). This should be done for a finite lattice system with N vertices. In order to get the zero-momentum limit of Eq. (24), we should first take into account that in Eq. (5) the integration over the zero-momentum elongations u_i is excluded since this corresponds to a translation of the solid. By carrying out the integration over the stress fields σ_{ij}, we obtain the zero-momentum limit of $H_{\rm def}[n]$,

$$\begin{aligned}\frac{H_{\rm def}(\mathbf{q}\to 0)}{k_BT} &= \frac{v_F}{N}\sum_{\mathbf{x},\mathbf{x}'} \frac{1}{2}\mu n_{12}(\mathbf{x})n_{12}(\mathbf{x}') + \mu n_{ii}(\mathbf{x})n_{ii}(\mathbf{x}') \\ &\quad + \frac{\lambda}{2} n_{ii}(\mathbf{x})n_{jj}(\mathbf{x}'). \end{aligned} \quad (29)$$

With the help of this expression, we can rewrite $Z_{\rm def}$ for $N\gg 1$ as

$$\begin{aligned} Z_{\rm def} &= \sum_{\mathcal{S}} \sum_{n_{ij}\in\mathcal{S}} \exp\left\{-\frac{1}{k_BT}[H_{\rm def}(n+\tilde{n}) + H_{\sigma^0}(n+\tilde{n})]\right\} \\ &= \sum_{\mathcal{S}} \sum_{n_{ij}\in\mathcal{S}} \exp\left[-\frac{H_{\rm def}(n)}{k_BT}\right]\exp\left[-4\pi^2\tilde{\beta}N\frac{n_1}{d_1}\frac{\sigma^0}{\tilde{\mu}}\right] \\ &\quad \times\exp\left[4\pi^2\tilde{\beta}N\left\{-\left[\left(\frac{n_1}{d_1}\right)^2 + \left(\frac{n_2}{d_2}\right)^2\right]\right.\right. \\ &\quad \left.\left. - \frac{\lambda}{2\mu}\left(\frac{n_1}{d_1}+\frac{n_2}{d_2}\right)^2\right\}\right], \end{aligned} \quad (30)$$

where n_i/d_i are determined by the equations

$$(2\mu+\lambda)\frac{n_1}{d_1} + \lambda\frac{n_2}{d_2} = -\sigma^0,$$

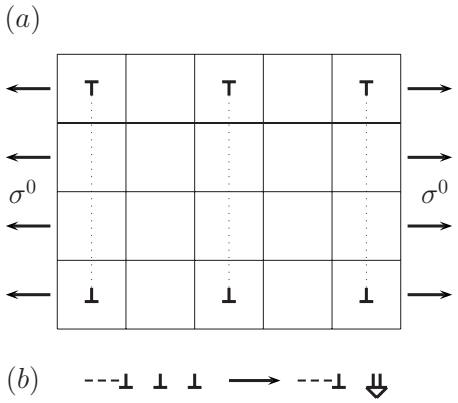

FIG. 3. In (a) we show a defect configuration $n_{ij}=\delta_{i1}\delta_{j1}\tilde{n}_{11}$ with $\tilde{n}_{11}$ as defined in Eq. (27) for $n_1=-1$ and $d_1=2$. (b) shows a dislocation pileup in a glide plane leading by merging of dislocations to a cleavage being the starting point of cracking.

$$(2\mu+\lambda)\frac{n_2}{d_2} + \lambda\frac{n_1}{d_1} = 0. \quad (31)$$

These equations ensure that all terms proportional to $\Sigma_{\mathbf{x}}\sigma^0_{ij}n_{ij}$ vanish in the exponent of Eq. (30). Solving them we obtain for n_j/d_j, with $j=1,2$,

$$\frac{n_1}{d_1} = -\frac{\sigma^0}{2\tilde{\mu}}, \quad \frac{n_2}{d_2} = \nu\frac{\sigma^0}{2\tilde{\mu}}. \quad (32)$$

These values simplify expression (30) to

$$Z_{\rm def} = \sum_{\mathcal{S}} \sum_{n_{ij}\in\mathcal{S}} \exp\left[-\frac{H_{\rm def}[n]}{k_BT}\right]\exp\left[-\frac{\tilde{H}^2_{\sigma^0}}{k_BT}\right]. \quad (33)$$

Finally we calculate $Z_{\rm def}$ for $\sigma^0=0$. Taking into account only the dominant defect configurations $n_{ij}(\mathbf{x}) \in \{\pm\delta_{i,1}\delta_{j,1}\delta_{\mathbf{x},\mathbf{x}_0}, \pm\delta_{i,2}\delta_{j,2}\delta_{\mathbf{x},\mathbf{x}_0}, \pm\delta_{i,1}\delta_{j,2}\delta_{\mathbf{x},\mathbf{x}_0}\}$, we obtain as in Refs. 22 and 23

$$Z_{\rm def}(\sigma^0=0) \approx \exp[2\exp(-6.3\tilde{\beta}) + 4\exp(-13.7\tilde{\beta})]. \quad (34)$$

From the considerations above we conclude that the cracking transition is in fact not a true phase transition in the Villain model but rather a crossover. The crossover temperature can be obtained by the assumption that the defect configurations $\tilde{n}_{11}$ or $\tilde{n}_{22}$ cover the whole crystal area at cracking, meaning that $d_i=1$. A defect configuration which covers only half of the crystal is shown in Fig. 3(a), where $n_{ij}=\delta_{i,1}\delta_{j,1}\tilde{n}_{11}$ with $n_1=-1$ and $d_1=2$. The idea behind this crossover temperature comes from the fact that most cracking transition models start with a pileup of dislocations within a glide where then by merging we obtain a cleavage dislocation being the start point of cracking.[27] This is shown in Fig. 3(b).

From Eq. (32) and the stability criterion[22] $|\nu|\leq 1$ we obtain that the lowest stress configuration where we have $d_i=1$ is given for $d_1=1$ and $n_1=1$ resulting in a cracking stress σ^0_b,

$$\frac{\sigma_b^0}{2\tilde{\mu}} = 1. \tag{35}$$

Comparing this value with the low-temperature cracking stress in the mean-field approximation of the cosine model given by $\sigma_b^0/2\tilde{\mu} \approx 0.33$ seen in Fig. 1, we obtain a much higher stress here. The relative strain in the crystal phase is given by $\Delta u_\parallel / a = k_B T \partial \ln[Z^{T\to 0}]/\partial(Nv\sigma^0)$ resulting in

$$\frac{\Delta u_\parallel}{a} = 2\frac{\sigma^0}{2\tilde{\mu}}. \tag{36}$$

Comparing Eq. (36) with the elastic part of the relative strain $\sigma^0/2\tilde{\mu}$, we obtain a factor of 2 difference. By using Eq. (36) with Eq. (35) we obtain a relative strain at cracking of 200% or $\Delta u_\parallel / a = 2$, respectively.

Let us now address the question whether the defect field configuration $\tilde{n}_{ij}$ of Eq. (27) is the only defect configuration leading to the partition function (33). The answer is negative. From the above derivation we see that *any* $\tilde{n}_{ij}$ arising from the substitution $n_{ij} \to n_{ij} + \tilde{n}_{ij}$ explained below Eq. (28) leads to Eq. (33) under the condition that $\tilde{n}_{11}(\mathbf{k})$ is only nonzero for $k_2 = 0$ and $\tilde{n}_{22}(\mathbf{k})$ for $k_1 = 0$. All these fields will be denoted as *defect vacuum*. Such $\tilde{n}_{ij}(\mathbf{x})$ correspond to defect stripes covering the whole width of the crystal where the $\tilde{n}_{ii}(\mathbf{k}=0)$ values are determined from the condition that the term proportional to $\Sigma_{\mathbf{x}} \sigma_{ij} n_{ij}$ vanishes in the partition function. From the thermodynamic point of view, none of the defect configurations $\tilde{n}_{ij}(\mathbf{x})$ which fulfill the above conditions are preferred. On the other hand we used the argument $d_i = 1$ for determining the cracking crossover stress (35) which was justified by the defect-merging picture in Fig. 3(b). Now suppose that we have additional external conditions in the crystal, for example, impurities or fixed crystal defects generated during crystal growth, which lead to the restriction that defects cannot cover the whole width of the system. Then the substitution $n_{ij} \to n_{ij} + \tilde{n}_{ij}$ cancels the term $\Sigma_{\mathbf{x}} \sigma_{ij} n_{ij}$ in Eq. (23) only partly. This is so since the exact cancellation relies on the fact that the only nonvanishing contribution of Eq. (28) in Eq. (24) is given by the $n_1 = n_2 = 0$ term, which has zero momentum. Finite-length defect stripes have this property only approximately. These also contribute to Eq. (24). Nevertheless, the partition function is still approximated by Eq. (33) if these residual terms are suppressed with respect to the term $\Sigma_{\mathbf{x}} \sigma_{ij} n_{ij}$. From Eq. (24) we see that Eq. (33) is best fulfilled under the stripe length restriction for that defect vacuum $\tilde{n}_{ij}$ which has the largest momentum region in the vicinity of $k_i = 0$, where $n_{ii}(\mathbf{k} \neq 0)$ is almost zero. These defect configurations consist of homogeneously distributed defect stripes in perpendicular direction where the density in this direction is determined from Eq. (32).

Note that the homogeneity can be only be fulfilled exactly for stresses $\sigma_0/2\tilde{\mu} \in 1/\mathbb{N}$. The average distance $d_i a$ between the stripes is then given by Eq. (32) for $n_i = 1$. The cracking condition $d_i = 1$ is again given by the fact that the homogeneously distributed defect stripes cover the whole crystal area where this criterion is justified by the defect-merging picture in Fig. 3(b). This leads immediately to the dimensionless cracking stress (35) and strain (36).

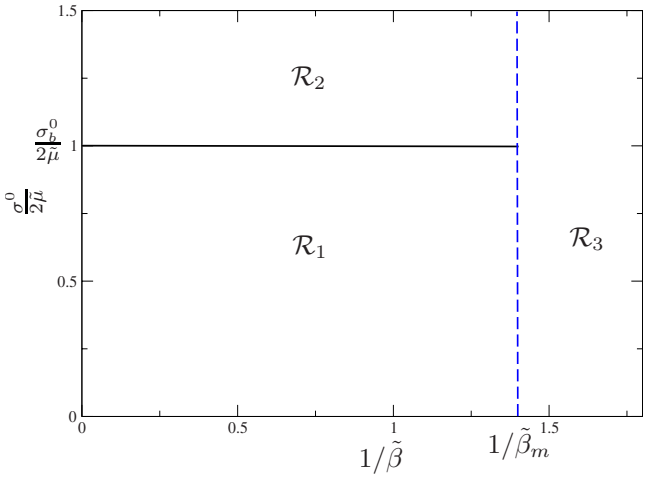

FIG. 4. (Color online) We show the low- and high-temperature intersection curve of the free energies given by Eq. (37) [(blue) dashed curve]. The (black) solid curve denotes the cracking transition line determined by Eq. (35).

Let us finally remark that the requirement of a homogeneously distributed defect stripe configuration as the vacuum is also in accordance with the conception that in real crystals the external homogeneous stress should be relaxed homogeneously across the area by defects.

We are now prepared to calculate the melting line by intersecting the partition functions of the low-temperature (17) and the high-temperature (21) expansions. The result is

$$\tilde{\beta} \exp[4 \exp(-6.3\tilde{\beta}) + 8 \exp(-13.7\tilde{\beta})] \exp[-4 \exp(-5/\tilde{\beta})] \approx 0.81 \tag{37}$$

independent of σ^0. The phase diagram is shown in Fig. 4. It displays the intersection line (37) of low- and high-temperature free energies [(blue) dashed curve] and the crossover cracking temperature (35) plotted as a (black) solid curve. We obtain from Fig. 4 that the melting temperature is given by $1/\tilde{\beta} \approx 1.42$. The melting line is given by a first-order transition in the case of a square lattice.[22,23] This was also found in Ref. 28 by using computer simulations.

V. PHASE DIAGRAM OF 2D CRYSTALS

So far we have obtained the phase diagram in Fig. 1 by applying a mean-field approximation in the cosine model of crystal defect melting and the phase diagram in Fig. 4 from the associated Villain-type model. The main difference lies in the fact that in the mean-field cosine model the cracking transition between the phases $\mathcal{R}_1$ and $\mathcal{R}_2$ is a second-order phase transition, but in the Villain-type defect model it is only a crossover. This and the differences in the value of the breaking stresses σ_b^0 have their origin in calculation of the cosine-model partition function in a mean-field approximation. It is a well-known phenomenon in many physical systems, especially in low dimensions, that quantum as well as thermodynamical fluctuations can destroy a phase transition which appears in a mean-field approximation, leaving only a

crossover. We have already mentioned an example for this in Sec. III with the 1D *XY* model.[26] Summarizing, we expect a similar phase diagram as in Fig. 4 for a real 2D crystal under stress. The stress-independent melting temperature in this figure is in accordance with the fact that in real physical systems there exists a melting transition beyond cracking. In a triangular lattice, we expect for the melting transition line two nearby Kosterlitz-Thouless transitions instead of the first-order transition found in the square lattice.[23,29]

In addition, our model was shown to possess a temperature-independent cracking transition line in Fig. 4 which is in agreement with the experimental determined cracking stress of 3D graphite in Ref. 30. In that experiment, the cracking stress σ_b^0 shows an anomalous temperature behavior only in a small temperature range just before melting where it starts to increase for larger temperatures. Such an increase in the cracking stress was also seen in other experiments where this increase starts even for smaller temperatures.[31] This behavior is not fully understood yet. That the cracking stress has a small temperature dependence is expected and should be revealed when going beyond the elastic lowest-order gradient expansion approximation used here when deriving the Villain lattice defect model. These approximations are released by using the iV approximation in Sec. III to the Villain lattice defect model,[22] leading to Hamilton terms beyond elasticity. This leads us to the possibility to determine the physics of real crystal models which are not restricted to the elastic lowest-order gradient expansion with the following conclusion: we expect a small temperature dependence of the cracking stress separating the phases $\mathcal{R}_1$ with $\mathcal{R}_2$ for realistic models. Nevertheless, the melting temperature transition separating $\mathcal{R}_2$ and $\mathcal{R}_3$ should not have a stress dependence also for more realistic models. Note that terms generated in the Hamiltonian beyond elasticity by using the iV approximation are in general not directly connected to higher-order terms of a certain real existing crystal.

In the following, we shall generalize our calculation of the last section to crystals with stresses irrespective of direction. In order to get the cracking stress, one has to repeat the calculation of Sec. IV where now $\tilde{n}_{ij}$ in Eq. (27) contains additionally a term of the form $n_{12}\delta_{i,1}\delta_{j,2}(\delta_{x_1,ad_{12}\mathbb{Z}}+\delta_{x_2,ad_{12}\mathbb{Z}})$. By carrying out the calculation, we obtain the same defect part of the partition function Z_{def} as in Eq. (33). The cracking transition is again determined by the minimal stress where $n_i/d_i=1$ or $n_{12}/d_{12}=1$, respectively. With this condition, we obtain for the cracking stress

$$\frac{\sigma_b^0}{2\tilde{\mu}} = \frac{1}{(1+\nu)} \min\left\{ \begin{array}{c} \left|\cos^2(\vartheta) - \dfrac{\nu}{1+\nu}\right|^{-1} \\ \left|\sin^2(\vartheta) - \dfrac{\nu}{1+\nu}\right|^{-1} \\ |\cos(\vartheta)\sin(\vartheta)|^{-1} \end{array} \right\}, \tag{38}$$

where we took into account $\sigma_{ij}^0 = \sigma^0[\cos(\vartheta),\sin(\vartheta)] \times [\cos(\vartheta),\sin(\vartheta)]$. Here ϑ is the angle between one crystal axis and the external force.

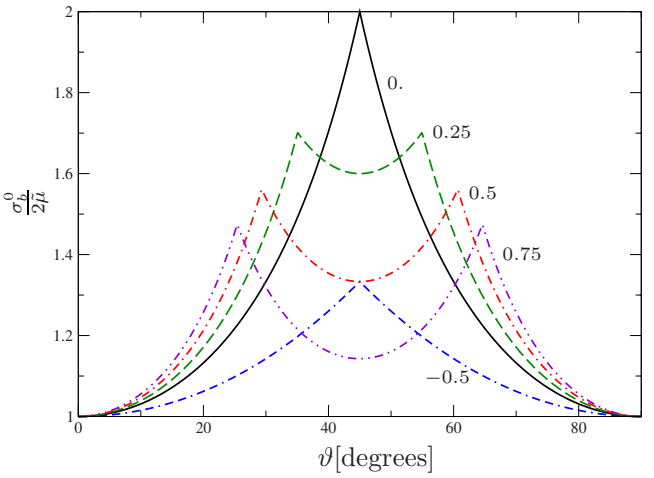

FIG. 5. (Color online) The figure shows $\sigma_b^0/2\tilde{\mu}$ (38) as a function of the angle ϑ between external force and the crystal axis ϑ. The numbers at the curves denote the Poisson ratio ν.

We may now calculate the relative strains orthogonal to the external force by inserting in Eq. (7) for σ_{ij}^0 an additional orthogonal auxiliary stress field in order to calculate the orthogonal strains by differentiation. This leads to relative strain values parallel to the external force $\Delta u_\parallel/a$ and orthogonal to it $\Delta u_\perp/a$ of

$$\frac{\Delta u_\parallel}{a} = 2\frac{\sigma^0}{2\tilde{\mu}}, \tag{39}$$

$$\frac{\Delta u_\perp}{a} = -2\nu\frac{\sigma^0}{2\tilde{\mu}}. \tag{40}$$

We show in Fig. 5 the dimensionless cracking stress $\sigma_b^0/2\tilde{\mu}$ (38) for certain Poisson ratios ν. Together with Eq. (39) we obtain parallel relative strains $\Delta u_\parallel/a \approx 200-400$ % where the concrete value depends on the Poisson ratio ν and angle ϑ. We note here once more that the relative strains (39) and (40) are only valid for high temperatures or large time scales such that activation barriers are no longer relevant in the crystal.

These large increases in the strain values at high temperatures are in accordance with observations of Huang *et al.*[11,12] for carbon nanotubes mentioned in the introduction of this paper. They found generally relative elongations which are at least five times higher at cracking than the tensile failure value at low temperature.[32]

VI. WRAPPED SQUARE CRYSTALS AND CARBON NANOTUBES

In the previous sections, we have examined the behavior of large square crystals under stress. In the sequel we shall examine the modifications brought about by considering wrapped versions of these. They form infinitely long thin tubes with a perimeter much larger than the lattice constant. Then the curve of the tube is irrelevant and the previous crystal model remains applicable.

First, we shall consider *achiral* square tubes. These are

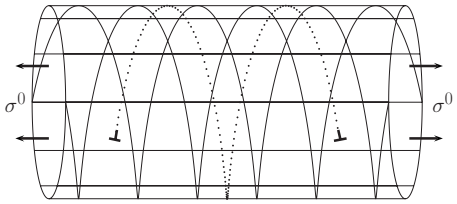

FIG. 6. We show a spiral-like defect configuration for a chiral square tube with $n_1=-1$ and $d_1=2$ by using the defect configuration (27). This defect configuration is consistent with the periodic boundary conditions around the circumference of the tube.

defined by the property that the vector along the circumference of the tube lies in the direction of a crystal axis leading to periodic boundary conditions in this direction. Due to the periodic boundary conditions along the crystal axis, after integrating out the zero-momentum strain fields described below Eq. (7), we obtain that the mean-field cosine results of Sec. III as well as the results for the Villain model of Secs. IV and V are also valid.

As described in the introduction section a *chiral tube* is defined by the property that the vector along the circumference of the tube lies not in the direction of a crystal axis. Thus the periodic boundary conditions after the integration of the homogeneous strain fields are no longer in the direction of a crystal axis but in the circumferential direction. The mean-field cosine results of Sec. III are of course still correct in this case. Also the cracking stress (38) and the strain-stress relations (39) and (40) are still valid. But the relevant defect configurations discussed below Eq. (36) are no longer homogeneously distributed stripes but spiral-like defect stripes. One such stripe is shown in Fig. 6. By cutting the tube along the axis and projecting it on the plane we, can use Eq. (27) with $n_i=n_{12}=1$ where we should further take into account $\tilde{n}_{12}$ defined in the last section. This generalization becomes relevant for external forces not directed along a square crystal axis valid for chiral tubes. The distances d_i and d_{12} between the stripes are determined by the periodic boundary conditions of the chiral tube. The number of defect stripes for every sort of defects $\tilde{n}_{ij}$ in axial direction is governed by the generalized equations of Eq. (31) used in Sec. V if we take into account also the defect field $\tilde{n}_{12}$. This means that we have to substitute in the generalized equation of Eq. (31) n_i/d_i and n_{12}/d_{12} by the defect density along the axis which is given by the number of stripes of a special defect type divided by the number of faces along the crystal axis. In general this leads to the result that the homogeneous distributed stripes do not cover the entire tube length.

In the uncut tube this defect configuration consists of long spiral-like defect stripes whose extension in the axial direction is as long as possible and consistent with Eq. (31). The reason lies in the fact that the substitution $n_{ij}\rightarrow n_{ij}+\tilde{n}_{ij}$ in Eq. (23) leads only to a cancellation of the external stress fields in the partition function when $\tilde{n}_{11}(\mathbf{k})$ is zero for $\mathbf{k}_2=0$ (and similar requirements for $\tilde{n}_{22},\tilde{n}_{12}$ as is outlined in Secs. IV and V). Only in this case the spiral-like defect configurations exactly cancel the external stress field in the partition function (23) as described in Sec. IV. Note that this requirement is exactly fulfilled only if a spiral-like defect covers the entire tube length. If a spiral-like defect stripe is smaller than the tube length where the generalized equation of Eq. (31) applies as described in the last paragraph, the resulting stress term in the partition function (23) leads only to negligible contributions in the free-energy density for infinite-length and large-perimeter tubes compared to the free-energy expressions in (30).

That the spiral-like configurations with the longest unbroken defect stripes which fulfill Eq. (31) are the most relevant defect configurations $\tilde{n}_{ij}$ is also obviously by the fact that this configuration has lowest energy $H_{\mathrm{def}}[\tilde{n}]+H_{\sigma^0}[\tilde{n}]$ [Eqs. (24) and (25)], where the zero-momentum part (29) is included in this expression.

Due to the generalized relations corresponding to Eq. (31), the length of the spiral-like defect stripes increases for increasing stresses, leading to kink propagation observed by Huang *et al.* for carbon nanotubes.[11,12] From definition (27) and its $\tilde{n}_{12}$ generalization in Sec. V, we deduce further that the spiral-like defect length motion of stripes $\tilde{n}_{11}$ and $\tilde{n}_{22}$ are glide motions, whereas the stripes $\tilde{n}_{12}$ move by climbs.[22] Both motions were observed in the superelongation experiments of carbon nanotubes at high temperatures.[12]

All this discussion leads us to the following scenario: when increasing the stress applied to the tube, a spiral-like defect for every defect type $\tilde{n}_i$ and $\tilde{n}_{12}$ becomes longer by climb or glide, respectively. When one of the defect stripes cover the entire tube length, a new spiral-like defect of the same type starts to be formed. This goes on up to the point when the tube is covered by defects. This is when cracking starts.

Let us end this section by discussing shortly the difference between carbon nanotubes and wrapped square crystals in this theoretical description. A carbon nanotube consists of a wrapped honeycomb lattice with two atoms per fundamental cell. Taking into account that the energy dispersion in the optical sector of the lattice displacements is negligible in comparison to the acoustical sector[33] leads to the result that it is sufficient to consider minimally coupled integer-valued defect fields only in the elastic Hamiltonian of the acoustic sector.[34] This then leads to a triangular lattice melting model since the honeycomb lattice has a triangular Bravais lattice. We have considered in Ref. 23 a defect melting model for the triangular lattice (1) for zero external stress in the simplest way. The strain-stress relations (39) and (40) remain of course still valid for carbon nanotubes since different lattice symmetries have no influence on the long-range behavior of the lattice like the zero-momentum strain-stress relations (39) and (40). Only the cracking stress (38) and the defect vacuum configurations are changed. As described above, defect configurations in a square crystal or its wrapped version consists of defect stripes which are directed along the crystal axes building in general spirals in chiral tubes. The same thing is true for the stress release in carbon nanotubes. In contrast to a square lattice, where every vertex cuts two inequivalent lines along the crystal axes, every vertex cuts in a triangular lattice three inequivalent lines. This leads to the fact that the number of inequivalent defect stripes in the triangular lattice is thus a factor of 3/2 larger than in the square lattice. By taking into account the defect-merging picture in Fig. 3(b) for cracking, we conclude that in carbon nanotubes

the cracking stress should be correspondingly larger than in square tubes. The stress release now takes place on a larger amount of different homogeneously distributed defect stripes. To be more specific, we expect in a first rough approximation for carbon nanotubes cracking stresses being in the average a factor of 3/2 larger than in square tubes. Note that this factor is similar to the ratio between the melting temperature of square crystals and triangular ones[23] as well as between honeycomb lattices and square crystals.[35] In the latter case, one has to take into account properly the definition of the elongation fields in the elastic acoustic Hamiltonian as a function of the atomic elongations[34] in order to obtain a temperature reduction factor at melting in comparison to the triangular lattice. A more elaborate treatment of the cracking stress of triangular or honeycomb lattice needs much more afford which is a work in progress.

VII. SUMMARY

Motivated by recent experiments revealing[11] that carbon nanotubes under external stress show a strong ductile behavior at high temperatures with extremely large relative elongations before cracking, we have calculated in this paper the phase diagram, the cracking stress, and the relative elongations of 2D square crystal lattices. By starting from a Villain-type lattice defect model, we have derived in Sec. II, using the inverse Villain approximation, an *XY*-like model for crystals. When calculating, within this model, the phase diagram in mean-field approximation in the (T,σ^0) plane, we have obtained two phase transition lines (see Fig. 1). There is a second-order transition at lower temperatures which we identified as the cracking transition line and a vertical second-order line indicating a melting transition beyond cracking. The dimensionless cracking stress $\sigma_b^0/2\tilde{\mu}$ as well as the relative strain rates parallel to the external force $\Delta u_\parallel/a$ has upper bounds of $\sigma_b^0/2\tilde{\mu} \leq 1/3$ and $\Delta u_\parallel/a \leq 2/3$ (see Fig. 2).

Next, we have calculated the phase diagram of the full Villain model within low- and high-temperature expansions of the free energy. Here we have found within the low-temperature expansion that the cracking transition is in fact not a phase transition but a crossover. The crossover line is identified by the requirement that the ground-state defect configuration under stress should cover the whole plane of the crystal. Within our model, the cracking stress is independent of temperature. By using the intersection criterion of the low- and high-temperature expansions of the free energy, we obtain a melting temperature which is independent of the external stress. The full phase diagram for external forces along one crystal axis is shown in Fig. 4.

We have deduced in Sec. V from the considerations above that a crystal under stress should show, in general, a phase diagram as in Fig. 4. The phase transition line in the cosine model observed within the mean-field approximation should vanish upon taking fluctuations into account, converting it into a crossover line as was shown in Sec. IV within the Villain lattice defect model. Nevertheless, we expect by going beyond the elastic lowest-order gradient expansion approximation used in the Villain model a small temperature dependence of the cracking stress, but no stress dependence of the melting transition temperature. This is motivated by the results for the cosine model of Sec. III since the iV approximation used to derive this model from the Villain model generates Hamilton terms beyond the elastic approximation.

Finally, we have calculated the cracking stress and the relative elongations before cracking. In Fig. 5 we have shown the resulting dimensionless cracking stress as a function of the angle between the external force and the crystal axes for various Poisson ratios. We have found dimensionless cracking stresses $\sigma_b^0/2\tilde{\mu}$ between 100% and 200% at high temperatures where potential barriers for defects are no longer relevant. The full relative strains $\Delta u_\parallel/a$ in the direction of the external force are twice as large as the elastic strain part. The reason lies in the defect degrees of freedom which then results in full relative strain rates $\Delta u_\parallel/a$ of 200–400 % at cracking depending on the direction of the external force and the Poisson ratio. The large difference in the cracking stresses and the strain rates between the mean-field result of the cosine model and the exact calculation of the Villain lattice defect model are presumably due to the mean-field approximation.

In Sec. VI we have obtained that the cracking stress relation (38) as well as the strain-stress relations (39) and (40) are also valid for wrapped square crystals. The defects are spiral-like for chiral tubes where defect glide and climbs are relevant in accordance with experiments. For honeycomb lattices or carbon nanotubes also the stress-strain relations (39) and (40) are fulfilled, but the cracking stress (38) is now modified. We have given arguments that cracking stresses in carbon nanotubes should be, on the average, larger than in square tubes by roughly a factor of 3/2.

ACKNOWLEDGMENT

The authors acknowledge the support provided by Deutsche Forschungsgemeinschaft under Grant No. KL 256/42-2.

[1] K. S. Novoselov, A. K. Geim, A. K. Geim, S. V. Morozov, D. Jiang, Y. Zhang, S. V. Dubonos, I. V. Grogorieva, and A. A. Firsov, Science **306**, 666 (2004).

[2] K. S. Novoselov, D. Jiang, F. Schedin, T. J. Booth, V. V. Khotkevich, S. V. Morozov, and A. K. Geim, Proc. Natl. Acad. Sci. U.S.A. **102**, 10451 (2005).

[3] J. C. Meyer, A. K. Geim, M. I. Katsnelson, K. S. Novoselov, T. J. Booth, and S. Roth, Nature (London) **446**, 60 (2007).

[4] D. R. Nelson and L. Peliti, J. Phys. (Paris) **48**, 1085 (1987).

[5] S. Iijima, Nature (London) **354**, 56 (1991).

[6] B. I. Yakobson, M. P. Campbell, C. J. Brabec, and J. Bernholc, Comput. Mater. Sci. **8**, 341 (1997).

[7] R. W. Haskins, R. S. Maier, R. M. Ebeling, C. P. Marsh, D. L. Majure, A. J. Bedna, C. R. Welch, B. C. Barker, and D. T. Wu, J. Chem. Phys. **127**, 074708 (2007).
[8] M. F. Yu, B. S. Files, S. Arepalli, and R. S. Ruoff, Phys. Rev. Lett. **84**, 5552 (2000).
[9] D. A. Walters, L. M. Ericson, M. J. Casavant, J. Liu, D. T. Colbert, K. A. Smith, and R. E. Smalley, Appl. Phys. Lett. **74**, 3803 (1999).
[10] M. Yu, O. Lourie, M. J. Dyer, K. Moloni, T. F. Kelly, and R. S. Ruoff, Science **287**, 637 (2000).
[11] J. Y. Huang, S. Chen, Z. Q. Wang, K. Kempa, Y. M. Wang, S. H. Jo, G. Chen, M. S. Dresselhaus, and Z. F. Ren, Nature (London) **439**, 281 (2006).
[12] J. Y. Huang, S. Chen, Z. F. Ren, Z. Q. Wang, D. Z. Wang, M. Vaziri, Z. Suo, G. Chen, and M. S. Dresselhaus, Phys. Rev. Lett. **97**, 075501 (2006).
[13] F. Ding, K. Jiao, M. W. Wu, and B. I. Yakobson, Phys. Rev. Lett. **98**, 075503 (2007).
[14] C. Tang, W. Guo, and C. Chen, Phys. Rev. Lett. **100**, 175501 (2008).
[15] P. Zhang, P. E. Lammert, and V. H. Crespi, Phys. Rev. Lett. **81**, 5346 (1998).
[16] B. I. Yakobson, Appl. Phys. Lett. **72**, 918 (1998).
[17] M. Buongiorno Nardelli, B. I. Yakobson, and J. Bernholc, Phys. Rev. Lett. **81**, 4656 (1998).
[18] D. Bozovic, M. Bockrath, J. H. Hafner, C. M. Leiber, H. Park, and M. Tinkham, Phys. Rev. B **67**, 033407 (2003).
[19] Q. Zhao, M. Buongiorno Nardelli, and J. Bernholc, Phys. Rev. B **65**, 144105 (2002).
[20] T. Dumitrică, M. Hua, and B. I. Yakobson, Proc. Natl. Acad. Sci. U.S.A. **103**, 6105 (2006).
[21] T. Dumitrică and B. Yakobson, Appl. Phys. Lett. **84**, 2775 (2004).
[22] H. Kleinert, *Stresses and Defects: Differential Geometry and Crystal Melting*, Gauge Fields in Condensed Matter Vol. II (World Scientific, Singapore, 1989); www.physik.fu-berlin.de/kleinert/re.html#b2
[23] J. Dietel and H. Kleinert, Phys. Rev. B **73**, 024113 (2006).
[24] D. R. Nelson, in *Statistical Mechanics of Membranes and Surfaces*, edited by D. Nelson, T. Piran, and S. Weinberg (World Scientific, Singapore, 2004).
[25] H. Kleinert, *Superflow and Vortex Lines: Disorder Fields and Phase Transition*, Gauge Fields in Condensed Matter Vol. I (World Scientific, Singapore, 1989); www.physik.fu-berlin.de/kleinert/re.html#b1
[26] G. S. Joyce, Phys. Rev. Lett. **19**, 581 (1967).
[27] J. P. Hirth and J. Lothe, *Theory of Dislocations* (John Wiley & Sons, Toronto, 1982).
[28] W. Janke and H. Kleinert, Phys. Lett. A **114**, 255 (1986); W. Janke and D. Toussain, *ibid.* **116**, 387 (1986).
[29] B. I. Halperin and D. R. Nelson, Phys. Rev. Lett. **41**, 121 (1978); D. R. Nelson and B. I. Halperin, Phys. Rev. B **19**, 2457 (1979); A. P. Young, *ibid.* **19**, 1855 (1979).
[30] L. M. Gillin, J. Nucl. Mater. **23**, 280 (1967).
[31] C. Malmstrom, R. Keen, and L. Green, J. Appl. Phys. **22**, 593 (1951); W. V. Kotlensky and H. E. Martens, Nature (London) **206**, 1246 (1965).
[32] J. Y. Huang, S. Chen, Z. F. Ren, Z. Q. Wang, K. Kempa, M. J. Naughton, G. Chen, and M. S. Dresselhaus, Phys. Rev. Lett. **98**, 185501 (2007).
[33] J. Maultzsch, S. Reich, C. Thomsen, H. Requardt, and P. Ordejón, Phys. Rev. Lett. **92**, 075501 (2004).
[34] H. Suzuura and T. Ando, Phys. Rev. B **65**, 235412 (2002).
[35] J. Dietel and H. Kleinert, Phys. Rev. B **79**, 075412 (2009).